Research Article Vol. 25, No. 9 | 1 May 2017 | OPTICS EXPRESS 10031

Optics EXPRESS

Nanoscale modeling of electro-plasmonic tunable devices for modulators and metasurfaces

CHRISTOPH A. RIEDEL,[1,2,*] KAI SUN,[1,2] OTTO L. MUSKENS,[2], CH DE GROOT[1]

[1] *Electronics and Computer Science, Faculty of Physical Sciences and Engineering, University of Southampton, Southampton SO17 1BJ, UK*
[2] *Physics and Astronomy, Faculty of Physical Sciences and Engineering, University of Southampton, Southampton SO17 1BJ, UK*
[*] *cr2a13@soton.ac.uk*

Abstract: The interest in plasmonic electro-optical modulators with nanoscale footprint and ultrafast low-energy performance has generated a demand for precise multiphysics modeling of the electrical and optical properties of plasmonic nanostructures. We perform combined simulations that account for the interaction of highly confined nearfields with charge accumulation and depletion on the nanoscale. Validation of our numerical model is done by comparison to a recently published reflective meta-absorber. The simulations show excellent agreement to the experimental mid-infrared data. We then use our model to propose electro-optical modulation of the extinction cross-section of a gold dimer nanoantenna at the telecom wavelength of 1550 nm. An ITO gap-loaded nanoantenna structure allows us to achieve a normalized modulation of 45% at 1550 nm, where the gap-load design circumvents resonance pinning of the structure. Resonance pinning limits the performance of simplistic designs such as a uniform coating of the nanoantenna with a sheet of indium tin oxide, which we also present for comparison. This large value is reached by a reduction of the capacitive coupling of the antenna arms, which breaks the necessity of a large volume overlap between the charge distribution and the optical nearfield. A parameter exploration shows a weak reliance on the exact device dimensions, as long as strong coupling inside the antenna gap is ensured. These results open the way for a new method in electro-optical tuning of plasmonic structures and can readily be adapted to plasmonic waveguides, metasurfaces and other electro-optical modulators.

OCIS codes: (230.2090) Electro-optical devices; (250.5403) Plasmonics; (240.6680) Surface plasmons; (250.4110) Modulators.

References and links

1. R. Kirchain and L. Kimerling, "A roadmap for nanophotonics," Nat. Photon. **1**, 303–305 (2007).
2. V. E. Babicheva, A. Boltasseva, and A. V. Lavrinenko, "Transparent conducting oxides for electro-optical plasmonic modulators," Nanophotonics **4** (1), 165–185 (2015).
3. J. A. Dionne, K. Diest, L. A. Sweatlock, and H. A. Atwater, "PlasMOStor: A metal-oxide-si field effect plasmonic modulator," Nano Lett. **9** (2), 897–902 (2009).
4. A. Melikyan, N. Lindenmann, S. Walheim, P. M. Leufke, S. Ulrich, J. Ye, P. Vincze, H. Hahn, Th. Schimmel, C. Koos, W. Freude, and J. Leuthold, "Surface plasmon polariton absorption modulator," Opt. Express **19**, 8855–8869 (2011).
5. V. J. Sorger, N. D. Lanzillotti-Kimura, R. M. Ma, and X. Zhang, "Ultra-compact silicon nanophotonic modulator with broadband response," Nanophotonics **1** (1), 17–22 (2012).
6. A. Olivieri, C. Chen, S. Hassan, E. Lisicka-Skrzek, R. Niall Tait, and P. Berini, "Plasmonic nanostructured metal-oxide-semiconductor reflection modulators," Nano Lett. **15** (4), 2304–2311 (2015).
7. C. Lin, A. S. Helmy. "Dynamically reconfigurable nanoscale modulators utilizing coupled hybrid plasmonics," Sci. Rep. **5**, 12313 (2015).
8. U. Koch, C. Hoessbacher, J. Niegemann, C. Hafner, and J. Leuthold, "Digital plasmonic absorption modulator exploiting epsilon-near-zero in transparent conducting oxides," IEEE Photon. J. **1** (1), 4800813 (2016).
9. Y. Yao, R. Shankar, M. A. Kats, Y. Song, J. Kong, M. Loncar, and F. Capasso, "Electrically tunable metasurface perfect absorbers for ultrathin mid-infrared optical modulators," Nano Lett. **14** (11), 6526–6532 (2014).

#284827 https://doi.org/10.1364/OE.25.010031
Journal © 2017 Received 30 Jan 2017; revised 10 Mar 2017; accepted 10 Mar 2017; published 21 Apr 2017

10. J. Park, J. Kang, X. Liu , and M. L. Brongersma, “Electrically tunable epsilon-near-zero (ENZ) metafilm absorbers,” Sci. Rep. **5**, 15754 (2015).
11. J. Park, J. Kang, S. J. Kim, X. Liu , and M. L. Brongersma, “Dynamic reflection phase and polarization control in metasurfaces,” Nano Lett. **17** (1), 407–413 (2017).
12. Y. Huang, H. Wai, H. Lee, R. Sokhoyan, R. A. Pala, Krishnan Thyagarajan, Seunghoon Han, Din Ping Tsai, and Harry A. Atwater, “Gate-tunable conducting oxide metasurfaces,” Nano Lett. **16** (9), 5319–5325 (2016).
13. E. Feigenbaum, K. Diest, and H. A. Atwater, “Unity-order index change in transparent conducting oxides at visible frequencies,” Nano Lett. **10** (6), 2111–2116 (2010).
14. M. Abb, Y. Wang, C.H. de Groot, and O. L. Muskens, “Hotspot-mediated ultrafast nonlinear control of multifrequency plasmonic nanoantennas,” Nat. Commun. **5**, 4869 (2014).
15. P. Guo, R. D. Schaller, J. B. Ketterson, R. P. H. Chang, “Ultrafast switching of tunable infrared plasmons in indium tin oxide nanorod arrays with large absolute amplitude,” Nat. Photon. **10**, 267–273 (2016).
16. G. D. Wilk, R. M. Wallace, and J. M. Anthony, “High-κ gate dielectrics: Current status and materials properties considerations,” Appl. Phys. **89** (10), 5243–5275 (2001).
17. N. Large, M. Abb, J. Aizpurua, and O. L. Muskens, “Photoconductively loaded plasmonic nanoantenna as building block for ultracompact optical switches,” Nano Lett. **10**, 1741–1746 (2010).
18. M. D. Losego, A. Y. Efremenko, C. L. Rhodes, M. G. Cerruti, S. Franzen, and J. Maria, “Conductive oxide thin films: Model systems for understanding and controlling surface plasmon resonance,” Appl. Phys. **106**, 024903 (1999).
19. S. V. Gaponenko, *Introduction to Nanophotonics* (Cambridge University, 2010).
20. X. Liu, J. Park, J. Kang, H. Yuan, Y. Cui, H. Y. Hwang, and M. L. Brongersma, “Quantification and impact of nonparabolicity of the conduction band of indium tin oxide on its plasmonic properties,” Appl. Phys. **105**, 181117 (2014).
21. H. W. Lee, G. Papadakis, S. P. Burgos, K. Chander, A. Kriesch, R. Pala, U. Peschel, and H. A. Atwater, “Nanoscale conducting oxide PlasMOStor,” Nano Lett. **14** (1), 6463–6468 (2014).
22. P. Mühlschlegel, H.-J. Eisler, O. J. F. Martin, B. Hecht, D. W. Pohl, “Resonant optical antennas,” Science **10**, 1607–1609 (2005).
23. J. C. Prangsma, J. Kern, A. G. Knapp, S. Grossmann, M. Emmerling, M. Kamp, and B. Hecht, “Electrically connected resonant optical antennas,” Nano Lett. **12**, 3915–3919 (2012).
24. J. Kern, R. Kullock, J. Prangsma, M. Emmerling, M. Kamp, and B. Hecht, “Electrically driven optical antennas,” Nat. Photon. **9**, 582–586 (2015).
25. K. Dopf, C. Moosmann, S. W. Kettlitz, P. M. Schwab, K. Ilin, M. Siegel, U. Lemmer, and H.-J. Eisler, “Coupled T-shaped optical antennas with two resonances localized in a common nanogap,” ACS Photon. **2** (11), 1644–1651 (2015).
26. C. Sire, S. Blonkowski, M. J. Gordon, and T. Baron, “Statistics of electrical breakdown field in HfO2 and SiO2 films from millimeter to nanometer length scales,” Appl. Phys. Lett. **5**, 2822420 (2007).
27. W. M. Haynes, “CRC handbook of chemistry and physics,” (CRC Press, 2017).
28. H. A. Mohamed,“The effect of annealing and ZnO dopant on the optoelectronic properties of ITO thin films,” J. Phys. D: ApplPhys. **40** 4234–4240 (2007).
29. J. S. Kim, F. Cacialli, A. Cola, G. Gigli, and R. Cingolani, “Increase of charge carriers density and reduction of Hall mobilities in oxygen-plasma treated indium-tin-oxide anodes,” Appl. Phys. Lett. **75**, 19–21 (1999).
30. D. L. Wood, Kurt Nassau, T. Y. Kometani, and D. L. Nash, “Optical properties of cubic hafnia stabilized with yttria,” Appl. Opt. **29**, 604–607 (1990).
31. P. B. Johnson and R. W. Christy, “Optical constants of the noble metals,” Phys. Rev. B **6** (12), 4370–4379 (1972).
32. J. Kim, A. Dutta, G. V. Naik, A. J. Giles, F. J. Bezares, C. T. Ellis, J. G. Tischler, A. M. Mahmoud, H. Caglayan, O. J. Glembocki, A. V. Kildishev, J. D. Caldwell, A. Boltasseva, and N. Engheta, “Role of epsilon-near-zero substrates in the optical response of plasmonic antennas,” Optica **3**, 339–346 (2016).
33. Y. Wang, M. Abb, S. A. Boden, J. Aizpurua, C.H. de Groot, and O. L. Muskens, “Ultrafast nonlinear control of progressively loaded, single plasmonic nanoantennas fabricated using helium ion milling,” Nano Lett. **13** (11), 5647–5653 (2013).
34. G. Frank and H. Köstlin, “Electrical properties and defect model of tin-doped indium oxide layers,” Appl. Phys. A **27** (4), 197–206 (1982).

---

1. Introduction

Nanoplasmonic components are of interest for their potential of achieving enhanced light-matter interaction through confinement of electromagnetic fields below the diffraction limit. Plasmonics has found its way into applications such as field-enhanced spectroscopy and sensing, near-field microscopy, and metasurfaces. In recent years, plasmonics is being considered as an emerging technology for optical modulation and switching. The need for low-latency and energy efficient data communication is driving a development aimed at replacing copper wires with optical interconnects [1]. On-chip integrated photonic circuits require new forms of control of light at length scales compatible with the footprint of traditional nanoelectronic circuits.

Due to their high near-field confinement, plasmonic structures are highly sensitive to their surrounding medium. This has driven the design of plasmonic electro-optical modulators where an external electric field changes the refractive index around the antenna and thus its resonance wavelength [2]. Electrical tuning of plasmonic devices has opened the door to new applications in optical circuits and tunable metasurfaces. Examples for such devices are hybrid waveguides with plasmonic coatings, which are switched by an applied bias between low absorption (on-state) and high absorption (off-state) [3–8]. Electrical modulation is also of great interest for the realization of tunable metasurfaces, such as thin film reflectors [9–12].

While there exists a variety of materials whose refractive index changes by application of an electric field, carrier modulation of transparent conducting oxides (TCOs) has been shown as one of the most promising methods for ultrafast electro-optical modulation [13–15]. TCOs such as indium tin oxide (ITO) and aluminum zinc oxide (AZO) have transition wavelengths in the near to far infrared where their optical properties switch from dielectric to metallic behavior. Accumulating and depleting carriers inside TCOs switches between those two states, drastically changing the resonance conditions of the plasmonic structure. To realize the charge modulation, the TCO is placed as the semiconductor inside a metal-oxide-semiconductor (MOS) capacitance structure. As metal contact, plasmonic materials such as gold and silver are typically chosen. The insulating oxide can be silicon dioxide, however alumina (Al_2O_3) or hafnia (HfO_2) are preferred due to their higher dielectric constants [16].

Detailed modeling of the performance of the nanoscale electro-plasmonic response is of importance to rationally design functional devices. The strong dependence of plasmonic resonances on nanometer-scale electronic distributions requires a scale of modeling that goes far below that of traditional photonics, and is similar to that used in semiconductor nanoelectronics. New multiphysics modeling capabilities and tools allow the detailed description of such device geometries treating their electrical and optical characteristics on an equal footing. Here, we present detailed numerical modeling of several electro-plasmonic devices. We compare our model to recent experimental work at mid-infrared wavelengths and find excellent agreement.

We use our validated model to simulate the electro-optical performance of plasmonic structures using carrier accumulation and depletion in ITO. We show that an ITO gap-loaded structure exhibits large normalized modulation amplitudes with moderate resonance shifts. The resonance shift occurs due to a reduction of the capacitive coupling of the two antenna arms, similar to a previously published study [17]. This surpasses the use of a uniform ITO sheet, which is limited by resonance pinning. Our structure can be used as both reflection-based or transmission-based modulator.

2. ITO carrier modulation

As a guideline for the numerical design, we regard the analytical description of a medium with changing carrier concentration. While our numerical simulations focus on the telecom wavelength of 1550 nm, this analytical study can readily be adapted to any desired wavelength.

In the visible and infrared regime, the transparent conductive oxide (TCO) can be assumed to have a quasi-free electron gas, and its relative permittivities to be described by a Drude model [18]:

$$\varepsilon = \varepsilon' + j\varepsilon'' \qquad \varepsilon'(\omega) = \varepsilon_\infty - \frac{\omega_p^2}{\omega^2 + \Gamma^2}. \tag{1}$$

The real part of the permittivity at a certain frequency $\omega = 2\pi c_0/\lambda$ depends on the permittivity at large frequencies ε_∞, the plasma frequency ω_p and the scattering constant Γ, the latter two being given by [19, 20]:

$$\omega_p^2 = \frac{Ne^2}{m^* \varepsilon_0} \qquad and \qquad \Gamma = \frac{e}{m^* \mu}, \tag{2}$$

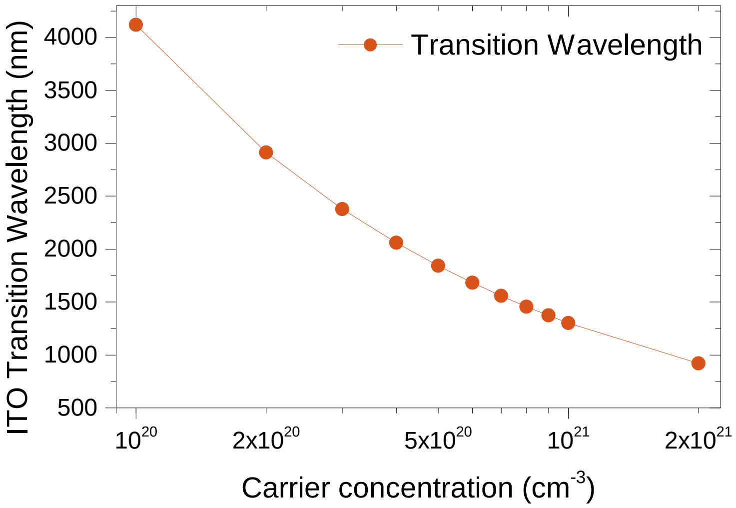

Fig. 1. Transition wavelength of ITO as a function of carrier concentration according to Eq. 3.

where N is the carrier concentration, m^* the effective electron mass, ε_0 the permittivity of vacuum, e the electron charge and μ the electron mobility. A material described by this model will switch from dielectric to plasmonic behavior at the transition wavelength where ε' changes sign. This is accompanied by a large change of the refractive index, which is why the epsilon-near-zero (ENZ) region has been identified as the key region for electro-optical modulation of plasmons [21]. As can be seen from equation 1, the value of ϵ' depends linearly on the carrier concentration of the material, and quadratically on λ. Therefore, to obtain a certain resonance shift at e.g. 1550 nm wavelength, the amount of carriers that have to be moved compared to 3100 nm is four times higher. This makes electrical modulation of optical properties at short wavelengths particularly challenging.

To find the wavelength at which epsilon transitions from positive to negative values, we rearrange Eq. 1 for λ, assume negligible losses and set $\varepsilon'(\omega) = 0$:

$$\lambda_{trans} = 2\pi \frac{c_0}{\omega_p} \times \sqrt{\varepsilon_\infty}. \tag{3}$$

This equation is plotted in Fig. 1. As can be seen, high carrier concentrations push the ENZ region towards shorter wavelengths. However, due to the inverse relation of N and λ_{trans}, it is challenging to approach the visible range. In this work, to model our ITO we use the values $\varepsilon_\infty = 4$, $m^* = 0.4 \times 9.11 \times 10^{-31}$ kg and $\Gamma = 1 \times 10^{14}$ rad s^{-1} [18]. These values are approximated to be constant over the carrier concentration ranges that occur. As shown by Liu et al [20], carrier concentrations above 1×10^{21} cm^{-3} cause an increase in m^*, which reduces the sensitivity of electrical modulation. We therefore compared our simulation results presented below using the Drude parameters of Liu et al with simulations using those of Park et al [10], which feature $m^* = 0.45 \times 9.11 \times 10^{-31}$ kg, finding negligible differences in performance.

3. Numerical methods

In the case of the electrical modulation of a TCO, carriers accumulate and deplete in a thin layer at the TCO-insulator interface. This can effectively be addressed by combined numerical simulations of both the electrical carrier distribution and the optical near-field response.

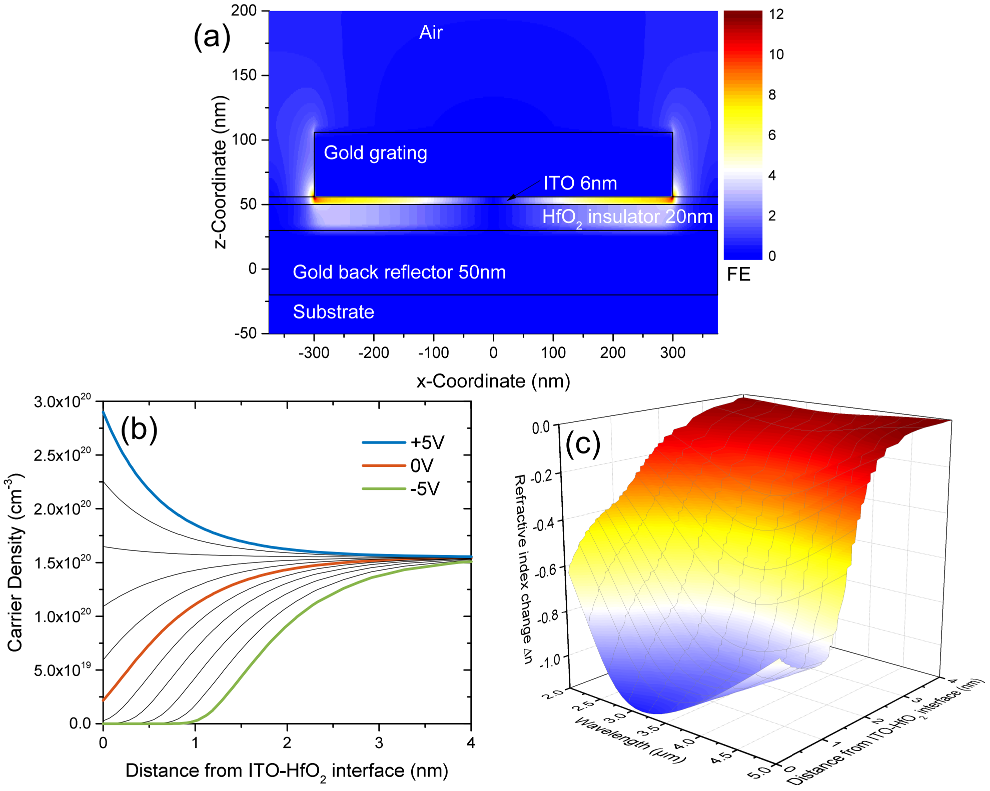

Fig. 2. Schematic and nearfield distribution at resonance of the structure by Park et. al [10]. The gold grating consists of infinitely long wires with 600 nm width and 750 nm period. (b) Simulated carrier distribution in a vertical line cut through the ITO using the software Lumerical DEVICE. (c) Induced refractive index change by changing the applied voltage from −5 V to +5 V as a function of wavelength and distance from the ITO-HfO$_2$ interface. At 3000 nm, the refractive index comes near zero close to the interface.

The structures were simulated using the optical and electrical solver of Lumerical Computational Solutions, Inc., FDTD and DEVICE. FDTD is an optical modeling tool that uses the finite-difference time domain (FDTD) method to compute light propagation and interaction with the resonant plasmonic structures. Carrier modulations can be implemented as refractive index perturbations of the TCO and are described using a Drude model as given in equation 1. DEVICE is a finite element method (FEM) solver that calculates carrier distributions and currents in a structure upon the application of an external bias. It iteratively solves the Poisson and the Drift-Diffusion equations. The solver assumes perfect insulators and perfect conductors, yet offers a detailed description of semiconductors in terms of electrostatic properties. The carrier distributions can be calculated in 3D or as 2D slices and then imported into FDTD where they are converted into refractive index perturbations.

To obtain accurate results, the mesh in both solvers has to be fine enough to accurately sample the carrier distribution curves. Careful tests showed that, in order to obtain smooth motion of the resonance peaks through the voltage steps, at least 10 mesh elements per charge layer were needed. In the case of carrier accumulation, where a layer thickness below 1 nm can be reached, this necessitates special care when setting up the electro-optical model. Figure 2(b) shows an exemplary charge distribution of the structure shown in Fig. 2(a), simulated using the DEVICE software. The charge modulation occurs in ITO upon the application of ±5 V over a 20 nm thick HfO_2 capacitance. At 0 V, a depletion layer of 1 nm is formed as a result of the different Fermi levels of the ITO and the gold contacts. Upon the application of a positive bias, charges accumulate up to a carrier concentration of $3 \times 10^{20}\,\mathrm{cm}^{-3}$ in a sub-1 nm thick layer. The negative bias causes depletion in a 1.5 nm thick layer.

The FDTD solver converts this charge distribution into refractive index distribution. To visualize the effect of the charge modulation, it is useful to calculate the charge difference between the depleted and accumulated case and convert it to a refractive index change by applying the Drude model. The resulting graph is plotted in Fig. 2(c) as a function of wavelength and distance from the insulator-semiconductor interface. The refractive index of depleted ITO is near $\varepsilon_\infty = 2$, while the background carrier density of $1.6 \times 10^{20}\,\mathrm{cm}^{-3}$ has an ENZ region at 4.2 µm which the carrier accumulation moves to 3 µm. The latter can be seen as the region of the largest refractive index reduction in the graph. At short wavelengths, the ITO is a dielectric ($\varepsilon' > 0$) while at wavelengths above 3 µm it behaves metallic ($\varepsilon' < 0$).

4. Validation of the numerical electro-optical model

To verify the accuracy of the combined electro-optical simulation capabilities and compare them to experimentally obtained spectra, we performed the modeling of the recently published electro-optical metasurface by Park et. al [10]. The structure consists of a gold grating that couples the incoming light to localized surface plasmons. A metal-insulator-metal (MIM) resonance is created between the grating, the layers of ITO and HfO_2 and the gold back reflector. The nearfield distribution at resonance is shown in Fig. 2(a). The application of an electrical bias of ±5 V changes the optical path length between the grating and the reflector by changing the carrier concentration of the intermediate 6 nm thick ITO layer.

Figure 3 shows the the experimental and simulated reflectance of the sample. For the simulations, all material parameters were taken from reference [10], except for the ITO carrier concentration, which was slightly increased from $1.47 \times 10^{20}\,\mathrm{cm}^{-3}$ to $1.6 \times 10^{20}\,\mathrm{cm}^{-3}$ to match the resonance wavelengths of the structure. The carrier distribution and resulting refractive index change are the ones from Fig. 2. The spectra show excellent agreement between experiment and simulation, especially in the formation of constructive and destructive interferences at different voltages. We obtain an absolute reflectance change of 13 percentage points and a normalized modulation of $\Delta R/R_0 = (R(V_+) - R(V_-))/R(0) = 21.5\%$ at 4.0 µm, while the experimental data show 14 percentage points and $\Delta R/R_0 = 25.7\%$ at 3.7 µm, respectively. The most prominent difference is an offset of the simulated graphs by 0.1 on the y-axis, which can be attributed to the lack of surface roughness and other fabrication imperfections in the model. An effect of the chosen Drude model parameters on the reflectance offset was not found.

5. Uniformly ITO-coated plasmonic nanoantennas

Electrical modulation of plasmonic nanoantenna dimers [22], contrary to stacked reflectors, poses peculiar challenges and opportunities. One opportunity is the small surface area of the antennas which makes them promising electrodes for low-capacitance structures. The direct electrical connection of nanoantenna arms has been characterized and utilized before and showed conservation of the antenna's optical properties [23,24]. By using the nanoantenna as an electrode, the unit cell area that contributes to the effective capacitance is below 1 $\mu\mathrm{m}^2$, enabling ultrafast electrical modulation due to the low RC constant.

One challenge on the other hand is the fact that dimer antennas are usually free standing and thus provide strong field enhancement only in the antenna gap. That makes it essential for the carrier modulation to occur in that region to get a large overlap between the electrical and optical response. Accumulating and depleting carriers homogeneously over a large area of TCO underneath the antennas is not sufficient.

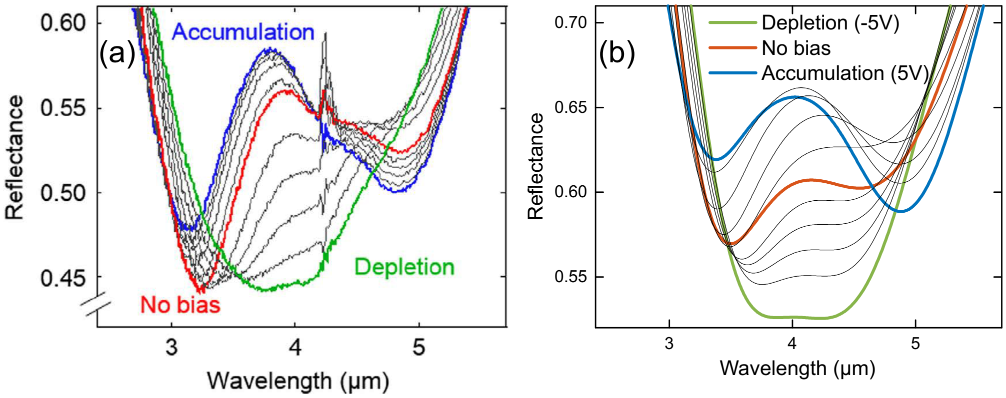

Fig. 3. Comparison between the measured and simulated reflectance of a reflective meta-absorber. (a) Measured optical reflectance using an FTIR, taken from [10] (under the Creative Commons License 4.0 `http://creativecommons.org/licenses/by/4.0/`). (b) Simulated reflectance from combined Lumerical DEVICE and FDTD simulations, showing good agreement with the experimental spectra.

In our simulations we use a wire mesh electrode which consists of gold dimer antennas, separated by a small gap, with each arm being electrically wired to a contact pad, see the top view in Fig. 4(a). Since the wires are orthogonal to the antenna arms, they do not couple to longitudinally polarized light, so that their optical response can easily be separated from the antennas [23, 25]. In the presented designs, the wires and antenna arms are modeled with a 30 nm×30 nm cross-section, which lies well within the capabilities of e-beam lithography.

To further specify issues that can arise when designing structures for plasmon-based electro-optical modulation, we give a simple three layer structure as an example. We regard the case of a uniformly coated nanoantenna dimer, which is shown in the schematic in Fig. 4(b). The schematic is a cut through the antenna arms of Fig. 4(a). The gold nanoantennas represent the bottom electrode, which is then coated by a 2 nm thick HfO_2 insulator and a 100 nm thick sheet of ITO. Via contact pads on the ITO, we apply a bias of ±2 V, which creates a carrier depletion at the ITO-HfO_2 interface [Fig. 4(c)]. The carrier sheet wraps around the antenna, giving two modulation layers inside the antenna gap, which provide the necessary overlap with the optical nearfield [Fig. 4(d)]. The ITO carrier density was set to $6.5 \times 10^{20}\,\mathrm{cm}^{-3}$, bringing the ITO ENZ region close to 1550 nm, where electrical modulation is strongest [12]. The antennas were designed to be 500 nm long and with a 30 nm gap to obtain a resonance at the telecom wavelength of 1550 nm.

In our simulations, we stay conservative with the maximum applicable electric field before breakdown. For HfO_2, breakdown voltages as high as $40\,\mathrm{MV\,cm}^{-1}$ have been reported [26], however only if the capacitance surface area remains as small as 10 nm. In our simulations we choose a more realistic electric field of $10\,\mathrm{MV\,cm}^{-1} = 1\,\mathrm{V\,nm}^{-1}$. In DEVICE, HfO_2 is characterized by its dielectric constant of 25 [16] and gold by its work function of 5.1 eV [27]. To model ITO, its bandgap was set to 4 eV, the dc dielectric constant to 9.3 and the work function to 4.5 eV [4, 28, 29]. In the optical solver, the refractive index of HfO_2 was set to 2.1 [30], while the optical constants for gold were taken from Johnson and Christy [31]. The optical constants of ITO were set according to the values given above.

In our simulations we will focus on the extinction cross-section of the antenna and how it can be modulated. The extinction cross-section is a fundamental antenna property defined as the ratio of the sum of the absorbed and the scattered power by the intensity of the incoming light $\sigma_{ext} = (A + S)/I$. The value we will give is the the normalized change in the extinction

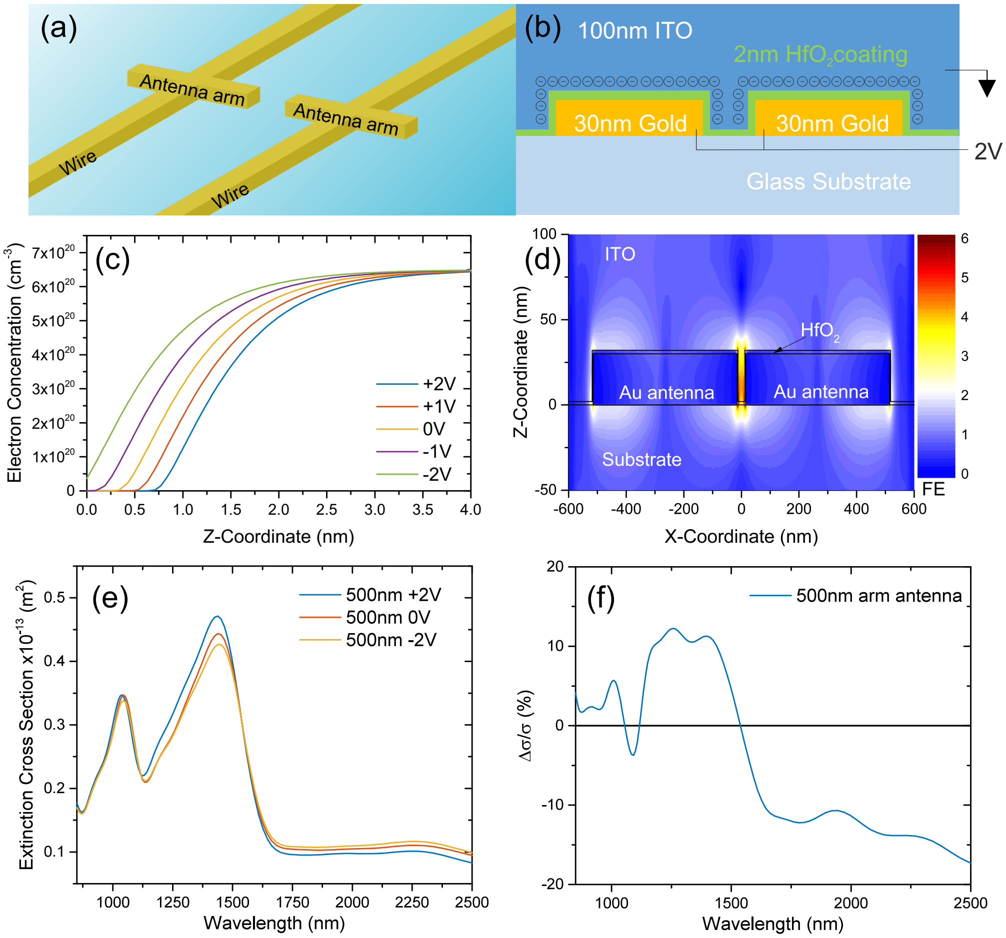

Fig. 4. (a) Schematic representation of a gold dimer antenna whose arms are electrically addressable by thin wires. (b) Cross-sectional view of the gold dimer antenna, coated by 2 nm of HfO_2 and 100 nm ITO. (c) Charge distribution inside the ITO upon the application biases from −2 V to +2 V. (d) Optical nearfield distribution of the proposed structure. The field enhancement (FE) is strongest in the gap and at the antenna ends. (e) Simulated extinction spectra of the depicted design, using an antenna with 500 nm arm length. (f) Normalized modulation from −2 V to +2 V by the same structure.

cross-section $\Delta\sigma/\sigma_0 = (\sigma(V_+) - \sigma(V_-))/\sigma(0)$. This allows an interpretation of the modulation strength of the structure. In a real experiment, the reflection and transmission will be the measured values. Modulation of these values depends on the exact device and experiment design. In some cases, such as when measuring a transmission dip for highly reflective antennas, relative changes can be huge while having low applicability. Showing extinction cross-section spectra avoids this issue.

The results for the uniformly coated nanoantennas are shown in Fig. 4(e). The $l_{eff} = \lambda/2$ resonance of the antenna is located at approx. 1550 nm,showing some amplitude modulation but no resonance shift. A second resonance ($l_{eff} = 3\lambda/2$) at 1100 nm does not show significant modulation. Above 1750 nm $\varepsilon'_{medium} < 0$ prevents the occurrence of any resonance due to the lack of a metal-dielectric interface. The ITO itself acts like a metal. In this spectral range, the baseline cross-section of 1×10^{-14} m^2 corresponds to the surface area of the antenna and the wires within one simulated unit cell. The spectrum of the normalized change in the extinction cross-section is given in Fig. 4(f).

The structure was designed with a focus on the effect of depletion, which shifts the refractive index towards higher values in the vicinity of the antenna. Depletion works in a larger volume than accumulation, thus providing a larger overlap with the antenna nearfield [Fig. 2(a)]. Therefore, a large red-shift of the antenna resonance is expected. However, as can be seen in the spectra, the resonance shift is countered by "resonance pinning" from the bulk ITO background close to ENZ. Resonance pinning describes the fact that a plasmonic nanostructure, which is surrounded by an ENZ material, loses sensitivity to small changes in its length or its surrounding medium [32]. Therefore, the structure shows mostly amplitude modulation, giving $\Delta\sigma/\sigma_0 = 11\%$ at 1550 nm. While this is a good value at this short wavelength, large scale resonance wavelength shifting cannot be realized with this simplistic structure.

6. ITO gap-loaded plasmonic nanoantennas

To circumvent the problem of resonance pinning, we introduce a gap-loaded antenna structure as depicted in Fig. 5(a). In this structure, instead of coating the whole structure with ITO, it is only deposited inside the antenna gap. The electrically connected rectangular antenna arms serve here as the top electrode. An ITO circle is deposited into the gap and acts as a switchable antenna load. The circle is 30 nm in diameter and 50 nm high. The carrier density was again chosen to be $6.5 \times 10^{20}\,\mathrm{cm}^{-3}$, to bring the ENZ region of the ITO close to the telecom wavelength. As back electrode, a low-doped transparent conductive oxide such as ITO is used, with a carrier density low enough to ensure the refractive index is constant over the investigated spectral window. The transparent electrode allows modulation of both the transmittivity and reflectivity of the sample. Additionally, it prevents coupling between the antenna arms and the back contact, thereby preserving the field enhancement in the gap. A potential disadvantage of the ITO back contact is that it will also accumulate and deplete charges. This is neglected at first, but addressed later.

Upon the application of a bias, charges accumulate at the bottom of the gap load. This reduces the capacitive coupling between the two antenna arms and results in a blue-shift of the antenna resonance. The abundance of ITO outside the gap prevents resonance pinning as observed in the previous structure. Because the gap-loaded antenna design was created with a focus on accumulation mode, a large HfO_2 thickness of 30 nm ensures that initial depletion of the ITO gap loading is low, see Fig. 5(b). This eases the formation of an accumulation layer upon the application of a positive bias. An advantage of a thicker insulating layer is the lower probability of breakdown due to pinholes compared to the 2 nm thick insulator in the uniformly ITO-coated structure. To maintain an electric field of $1\,\mathrm{Vnm}^{-1}$, a bias of ±30 V is required.

The extinction cross-section of this structure with and without the application of a bias are given in Fig. 5(c) for two different antenna arm lengths. Upon depletion, the resonance shows a small red-shift, which comes from the increased refractive index at the bottom of the gap load. Upon accumulation, the blue-shift occurs accompanied by a decrease in extinction cross-section. This is because upon crossing the ENZ condition, the bottom layer of the ITO gap load becomes metallic and thus creates a conductive bridge between the two antenna arms. This reduces capacitive coupling between the antenna arms efficiently, leading to the observed blue-shift. Similar results have been shown for other dimer antennas with varying gap-loading [17,33].

Fig. 5(d) shows the normalized modulation spectra. For an antenna arm length of 210 nm, we obtain a 0 V resonance peak at 1550 nm, which is shifted by 38 nm in wavelength and $\Delta\sigma/\sigma_0 = 15\%$ in amplitude. Yet, an even higher modulation is achieved on the long-wavelength side of the resonance. By reducing the antenna arm length to 160 nm, we utilize this to achieve a normalized modulation of $\Delta\sigma/\sigma_0 = 44.8\%$ at 1550 nm. We also note a large full-width at half-maximum of 526 nm. These promising results show the potential of our method to enable

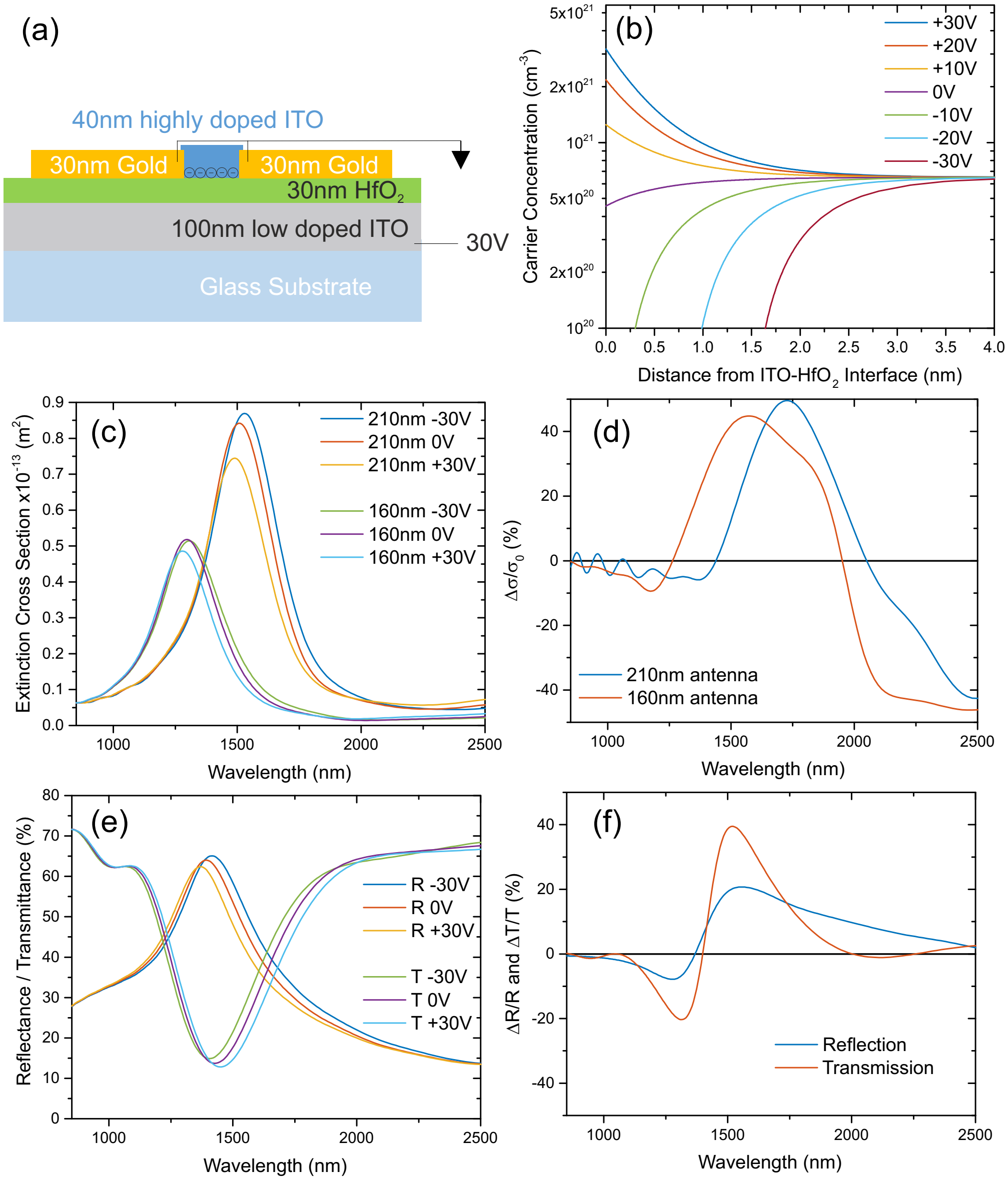

Fig. 5. (a) Cross-sectional view of the gap-loaded structure, where the substrate is coated by a back contact consisting of 100 nm low-doped ITO and 30 nm of HfO_2. The gold dimer antenna serves as top electrode and has a gap load of 50 nm high ITO. The top-view of the structure is the same as in Fig. 4(a). (b) Carrier distribution inside the ITO gap-load as a function of voltage. The accumulated carriers reach 3×10^{21} cm^{-3}. (c) Simulated extinction spectra of the depicted design, for antennas with 210 nm and 160 nm arm lengths. (d) Relative modulation of the same antennas normalized to the unperturbed cross-section spectrum. (e) Transmission and reflection spectra of a periodic structure with 250 nm transverse spacing between the antenna arms. (f) Normalized modulation of the spectra in (e).

strong modulation of free standing dimer nanoantennas at telecom wavelengths. To ease comparison with devices from other authors, we also simulated the reflection and transmission of a periodic antenna array, which is given in Fig. 5(e). In longitudinal direction, the array consists of an infinite row of 160 nm long antenna arms, separated by 10 nm gaps which are loaded with ITO as before. In transverse direction, the antenna rows have a 250 nm spacing. In our simulations, we found that spacings above 200 nm are sufficient to prevent resonance broadening through coupling. The normalized spectra for this structure are shown in Fig. 5(f), showing good modulation values up to $\Delta T/T_0 = 40\%$ in transmission. As mentioned above, the actual measured changes in reflection and transmission will depend on the final device structure, while the aim of this article is the presentation of the modulation mechanism itself. We will therefore focus on the extinction cross-section modulation.

The method depicted here, i.e. the reduction of capacitive coupling via an electrically switched $\varepsilon < 0$ layer of TCO, can be readily adapted to other structures, such as metasurfaces and plasmonic waveguides, opening up a new way of electrical control over optical properties. Naturally, the method can also be applied to other wavelength ranges by adjusting the antenna arm length and the initial ITO carrier concentration. The only limit in terms of the shortest wavelength where modulation is still achievable is the maximum carrier concentration obtainable by current deposition methods. For demonstrated carrier concentrations of e.g. $1\times10^{21}\,\mathrm{cm}^{-3}$ [34], the ENZ wavelength of ITO is at 1300 nm, which is approaching the visible regime.

Due to the nature of our gap-loaded approach, the antenna preserves many of its characteristic properties, such as the sub-1 µm footprint and the high field confinement at the antenna ends. The latter are largely unaffected by the gap-load, so that they can be used for plasmonic sensing and near-field enhanced nonlinear effects.

7. Sensitivity analysis

We further investigate the influence of the design parameters on the performance of the device to quantify the influence of fabrication imperfections. Figure 6 shows four graphs in each of which one design parameter is swept across several values. In Fig. 6(a) we show the electro-optical modulation performance for carrier concentrations from $2 \times 10^{20}\,\mathrm{cm}^{-3}$ to $1 \times 10^{21}\,\mathrm{cm}^{-3}$ inside the gap. As a general trend, a higher gap loading results in a small blue-shift of the unbiased resonance (not shown). In the normalized modulation spectra, we observe two peaks A (marked in black) and B (marked in red), where A is close to the resonance and B further toward the infrared. With increasing carrier concentration, peak A increases until reaching a maximum for a carrier concentration of $6.5 \times 10^{20}\,\mathrm{cm}^{-3}$. Further increase of the carrier concentration decreases the modulation peak again and narrows the modulation bandwidth. Peak B has opposite proportionality, with an increasing carrier concentration leading to a decrease in peak height. Due to the fact that B is far off the resonance [cp. Fig. 5(b)], this peak has limited usability. We conclude that a carrier concentration of $6.5 \times 10^{20}\,\mathrm{cm}^{-3}$ or higher is necessary to obtain modulation values above 40% near resonance at 1550 nm.

Figure 6(b) shows a sweep over the HfO_2 insulator thickness. We consider a thickness range from 10 nm to 50 nm and keep the electric field constant at $1\,\mathrm{Vnm}^{-1}$ to analyze in which condition the carrier accumulation works most effectively. From 30 nm to 50 nm the modulation is equally high around 44%, however a slight reduction can be observed for a lower insulator thickness. The modulation strength reduces to 42% at 1637 nm for 20 nm and 40% at 1664 nm for 10 nm. Since the total switching voltage scales linearly with HfO_2 thickness, this shows that effective resonance modulation is also possible at lower voltages.

A critical parameter of our design is the gap width of the antenna arms. The modulation spectra of gap widths from 10 nm to 100 nm are shown in Fig. 6(c). A gap width of 10 nm shows by far the highest modulation, due to the high near-field confinement inside the gap. Larger gaps up to 50 nm still give modulation, however with reduced values of $\Delta\sigma/\sigma_0 = 20\%$. Gaps of 100 nm or

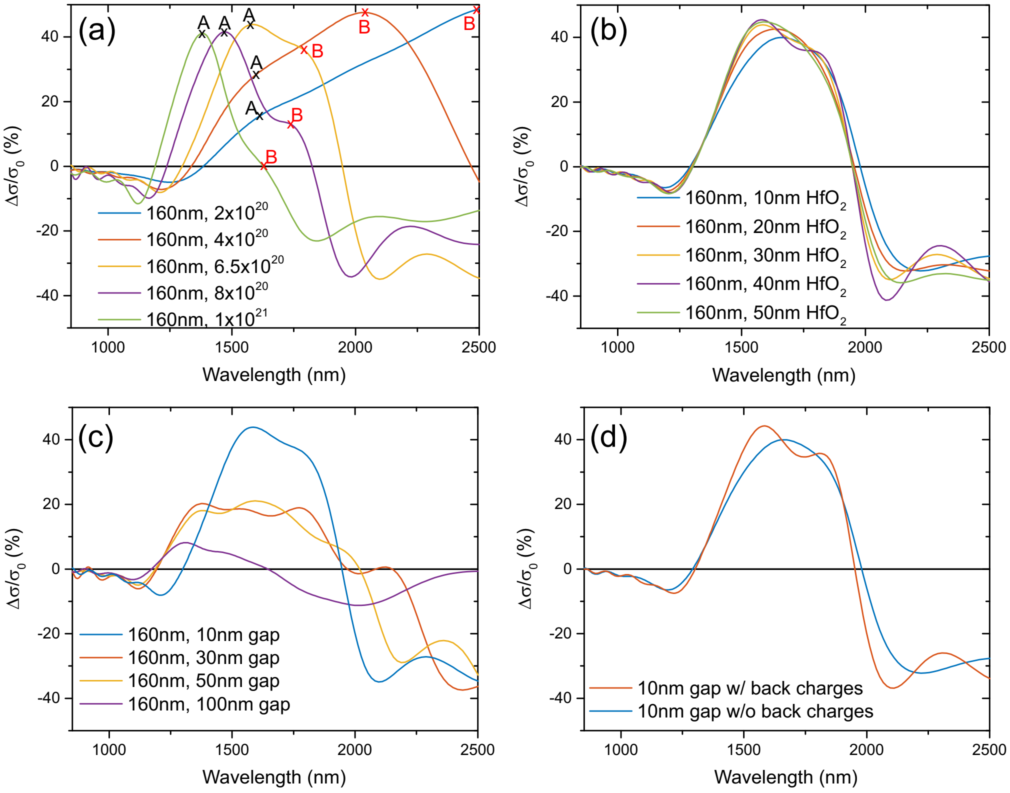

Fig. 6. (a) Normalized modulation spectra as a function of the carrier concentration of the gap load. The spectra show two main peaks, marked *A* in black and *B* in red. (b) Influence of the HfO_2 thickness on the peak modulation. (c) Influence of the antenna gap width on the modulation strength. (d) The modulation spectra with and without the inclusion of charge modulation in the low-doped ITO back contact.

higher should be avoided due to the reduced sensitivity of the antenna to gap loading. Finally we compare the modulation spectra with and without taking charges at the back contact into account [Fig. 6(d)]. For negative bias, the low-carrier ITO at the back contact experiences charging up to the order of 1×10^{21} cm^{-3}, counteracting the depleted gap-load. However due to the difference in near-field enhancement between the gap and the area below the antenna, the charges cause only a small perturbation of the modulation peak.

8. Conclusion

We have developed a numerical electro-optical model that describes the nanoscale electro-plasmonic response of nanoantenna switches. The model by far surpasses the capabilities of analytical models in predicting the detailed optical modulation spectra. Our model was compared with recent experimental results of the infrared resonances of a reflective meta-absorber under applied bias, obtaining excellent agreement in the optical resonance structure and modulated spectra. To find novel approaches in implementing plasmonic electro-optical modulation, we adapted our model to a geometry of gold dimer nanoantennas under an electrical bias. Two electrical modulation schemes were presented, the first one using a uniform ITO sheet on top of the antennas showing an amplitude modulation of 11%. The wavelength shift obtained in this case was limited by resonance pinning due to the ITO background. Our second proposed structure

Optics EXPRESS

confines the ITO to a circular gap load, leading to a normalized relative modulation amplitude of 45% at 1550 nm and a resonance shift of 28 nm. The resonance shift is caused by a reduction of the capacitive coupling of the antenna arms due to the highly conductive accumulation layer in the ITO. An additional parameter sweep shows that the structure is insensitive to changes of most parameters, as long as the antenna arms stay strongly coupled. These results open up a new way of realizing a scalable electro-plasmonic modulation platform that can easily be tuned to any desired wavelength by adjusting the antenna arm length and the ITO carrier concentration. It can also be adapted as an additional effect to existing waveguide structures and metasurfaces. Another advantage is the possibility to implement it as a transmission-based modulator.

Acknowledgments

This work acknowledges financial support by EPSRC through the research grant EP/J011797/1. The data for that was used for this work is accessible through the University of Southampton Institutional Research Repository (DOI: 10.5258/SOTON/405054).